



Cite this: *J. Mater. Chem. C*, 2015,  
3, 8225

# Optoelectronic properties and polar nano-domain behavior of sol–gel derived $K_{0.5}Na_{0.5}Nb_{1-x}Mn_xO_{3-\delta}$ nanocrystalline films with enhanced ferroelectricity

Qinglin Deng, Jinzhong Zhang, Ting Huang, Liping Xu, Kai Jiang, Yawei Li, Zhigao Hu\* and Junhao Chu

High-quality lead-free piezoelectric  $K_{0.5}Na_{0.5}Nb_{1-x}Mn_xO_{3-\delta}$  (KNNM $x$ ,  $0 \leq x \leq 0.10$ ) films have been successfully deposited on Pt(111)/Ti/SiO<sub>2</sub>/Si(100) substrates by a modified sol–gel method. The effects of Mn substitution on the microstructure, morphology, lattice vibrations, and optical and ferroelectric properties of the KNNM $x$  films have been investigated in detail. All films are polycrystalline, crack-free and show a pseudo-cubic (pc) structure with a thickness of about 215 nm. Raman analysis indicates that the characteristic frequency of  $\nu_1$ ,  $\nu_5$  and  $\nu_1 + \nu_5$  modes shifts towards lower wavenumbers with increasing Mn concentration. The optimal ferroelectric properties were obtained in the film doped with  $x = 0.06$ , whose remnant polarization ( $2P_r$ ) and coercive field ( $2E_c$ ) values at the applied electric field of  $1000 \text{ kV cm}^{-1}$  are  $51 \mu\text{C cm}^{-2}$  and  $265 \text{ kV cm}^{-1}$ , respectively. The increased valence of  $Mn^{2+}$ , which is substituted at the  $Nb^{5+}$  site as  $Mn^{3+}$ , plays an important role in reducing the amount of both oxygen vacancies and holes. In addition, the dielectric functions of the KNNM $x$  films have been uniquely extracted by fitting ellipsometric spectra with the Adachi dielectric function model and a four-phase layered model (air/surface rough layer/KNNM $x$ /Pt) in the photon energy range of 1.5–5.5 eV. The optical band gap ( $E_g$ ) slightly decreases, while the high-frequency dielectric constant ( $\epsilon_{\infty}$ ) linearly increases with increasing Mn concentration. Moreover, temperature dependent optical dispersion behavior of the KNNM0.06 film has been investigated from 300 K to 800 K. The analysis of  $E_g$  and the extinction coefficient ( $\kappa$ ) reveals the correlation between optical properties and structural phase transition. Furthermore, a distinct in-plane ( $180^\circ$ ) polar nano-domain pattern with a well-defined rectangular phase hysteresis loop has been observed in the KNNM0.06 film from piezoresponse force microscopy (PFM) experiments. The present results could be crucial for potential multifunctional KNN-based device applications.

Received 27th May 2015,  
Accepted 2nd July 2015

DOI: 10.1039/c5tc01514f

www.rsc.org/MaterialsC

## 1 Introduction

Until now, the most widely used piezoelectric materials have been Pb(Zr,Ti)O<sub>3</sub> (PZT)-based ceramics, which are famous for their remarkable piezoelectric response but contain a large amount of lead. Owing to the notorious toxicity of the lead element, these lead-based materials raise environmental and health concerns, limiting their development in many fields, such as biology and medicine.<sup>1–4</sup> Interest in effective alternatives to PZT-based materials has surged in order to create lead-free piezoelectric materials with properties that closely match those of the PZT family. Among them, the  $K_{0.5}Na_{0.5}NbO_3$  (KNN)-based system has been recognized as one of the most promising candidates due to some evident advantages, such as its relatively

high Curie temperature ( $T_C \sim 420 \text{ }^\circ\text{C}$ ), excellent ferroelectric and piezoelectric properties ( $d_{33} \sim 416 \text{ pC N}^{-1}$ ), as well as good biocompatibility.<sup>5–7</sup>

Most of the current research on KNN is for bulk ceramics and single crystals.<sup>5,6,8,9</sup> However, there are a few reports on KNN films, which could offer an unexceptional way to build miniaturized devices, such as sensors and micro-electromechanical systems (MEMS). KNN films have been prepared by various methods, such as pulsed laser deposition (PLD), RF-magnetron sputtering and the sol–gel method.<sup>10–12</sup> Among them, the sol–gel method is a well-accepted method due to some evident advantages, such as its chemical homogeneity, ease of stoichiometry control, low-cost and suitability for mass production.<sup>4,13</sup> Unfortunately, the sol–gel derived KNN films show disappointing ferroelectric and piezoelectric properties due to their high leakage current. Many studies have suggested that the oxygen and alkali-ion vacancies in perovskite oxides play a significant role in the high leakage current.<sup>14,15</sup> Doping different elements was frequently

Key Laboratory of Polar Materials and Devices, Ministry of Education, Department of Electronic Engineering, East China Normal University, Shanghai 200241, China.  
E-mail: zghu@ee.ecnu.edu.cn; Fax: +86-21-54345119; Tel: +86-21-54345150

adopted to effectively decrease the leakage current. Manganese (Mn) element is one of such dopants, which has been introduced into BaTiO<sub>3</sub>,<sup>16</sup> BiFeO<sub>3</sub>,<sup>17,18</sup> as well as KNN single crystals.<sup>8</sup> Although there are a few reports on the excellent ferroelectric and piezoelectric properties of Mn-doped KNN films, they were based on relatively thick films that are in the micrometer size range and did not show the optimal doping amount of Mn element.<sup>12,19</sup> It is a challenge to prepare high-quality thinner Mn-doped KNN films with the thickness on the nanometer scale, which can also show excellent ferroelectric and piezoelectric properties. In addition, the electrical properties of sol-gel derived Mn-doped KNN films have been the most extensively studied, while other physical properties, such as microstructure, lattice vibrations, leakage current mechanisms and ferroelectric domain behavior, need further clarification for potential applications. Moreover, in consideration of the few reports on the optical properties of KNN films, especially the study on ellipsometric spectra, investigation of its electronic band structure is urgently needed for future applications of optoelectronic devices. Note that spectroscopic ellipsometry (SE) is a powerful and nondestructive tool that allows us to simultaneously obtain the thickness and optical parameters of a multilayer system without Kramers-Krönig transformation (KKT).<sup>15,20</sup>

In this work, we devote major efforts to the preparation of high-quality thinner Mn-doped KNN films and determine the optimal doping amount of Mn element. Furthermore, the effects of Mn substitution on the microstructure, morphology, phonon modes and ferroelectric properties were investigated in detail. Besides, piezoresponse force microscopy (PFM) techniques were utilized to discuss the domain behavior. Optical properties were investigated in detail by SE. The Adachi dielectric function model and the four-phase structure were used to fit the ellipsometric spectra for extracting optical parameters. It is believed that the present work could be helpful in developing potential multifunctional KNN-based device applications, such as ferroelectric memory, ultraviolet detector and electro-optic devices.

## 2 Experimental section

### 2.1 Fabrication of KNNM<sub>x</sub> (0 ≤ x ≤ 0.10) films

K<sub>0.5</sub>Na<sub>0.5</sub>Nb<sub>1-x</sub>Mn<sub>x</sub>O<sub>3-δ</sub> (KNNM<sub>x</sub>, x = 0, 0.02, 0.04, 0.06, 0.08 and 0.10, or in short, KNNM0, KNNM0.02, KNNM0.04, KNNM0.06, KNNM0.08 and KNNM0.10, respectively) films were directly deposited on Pt(111)/Ti/SiO<sub>2</sub>/Si(100) substrates by a modified sol-gel method. Raw materials of sodium acetate (CH<sub>3</sub>COONa, 99.0%), potassium acetate (CH<sub>3</sub>COOK, 92.0%), manganese acetate [(CH<sub>3</sub>COO)<sub>2</sub>Mn·4H<sub>2</sub>O, 99.0%] and niobium ethoxide [(CH<sub>3</sub>CH<sub>2</sub>O)<sub>5</sub>Nb, 99.9%] were mixed in stoichiometric composition. Acetic acid (CH<sub>3</sub>COOH, 99.5%) and 2-methoxyethanol (CH<sub>3</sub>OCH<sub>2</sub>CH<sub>2</sub>OH, 99.0%) were used as solvents. Acetylacetone (CH<sub>3</sub>COCH<sub>2</sub>COCH<sub>3</sub>, 99.0%) was used as a chelating agent. Note that all of the chemical reagents and solvents used in the experiment were purchased from commercial sources and of analytical grade without any further purification. To compensate for the loss of alkaline metals during thermal annealing,

10 mol% K and Na excess were added to precursor solutions. All KNNM<sub>x</sub> precursor solutions were stirred using a magnetic stirrer in a constant temperature bath. Then they were adjusted to 0.2 mol L<sup>-1</sup> and filtered by using a 0.22 μm pore size filter. To obtain KNNM<sub>x</sub> films, the precursor solutions were spin-coated onto the Pt(111)/Ti/SiO<sub>2</sub>/Si(100) substrate. Prior to deposition, the substrates need to be cleaned in pure acetone and ethanol in an ultrasonic bath to remove oily substances and other impurities from the surfaces, followed by rinsing several times with deionized water, then the substrates were dried in a pure nitrogen stream. The films were deposited by employing a spin-coating process at a speed of 4000 rpm for 20 s. Each layer of the films was dried at 200 °C for 200 s to evaporate the solvent and then pyrolyzed at 380 °C for 200 s to remove residual organic compounds, followed by annealing at 680 °C for 300 s to crystallize the films by a rapid thermal annealing procedure. The spin-coating and annealing-treatment procedures were repeated ten times to obtain the desired thickness.

### 2.2 Characterization methods

The crystalline structure of the KNNM<sub>x</sub> films was analyzed by using a glancing angle X-ray diffractometer (XRD, D/MAX-2550V, Rigaku Co.) operated at 40 kV and 200 mA to exclude the effect of substrates. Raman scattering experiments were carried out using a micro-Raman spectrometer (Jobin-Yvon LabRAM HR 800UV) equipped with a 633 nm He-Ne laser as the exciting light. X-ray photoelectron spectroscopy (XPS) measurements were carried out on a RBD upgraded PHI-5000C ESCA system (Perkin-Elmer) with Mg-Kα radiation ( $h\nu = 1253.6$  eV), and binding energies were calibrated with respect to carbon contamination (C 1s = 284.6 eV). The cross-sectional images of all films were examined by field emission scanning electron microscopy (FESEM: Philips XL30FEG). Surface morphology and domain behavior of the KNNM<sub>x</sub> films were investigated by atomic force microscopy (AFM: Digital Instruments Icon, Bruker) in its ScanAsyst and PFM modes, respectively. The Co/Cr coated conductive PFM probes (Model: MESP) with a nominal force constant of 1–5 N m<sup>-1</sup> were used to analyze domain behavior. Platinum (Pt) dots with the diameter of about 0.2 μm deposited by a sputtering technique using a shadow mask are used as top electrodes for electrical measurements, while the Pt layer served as a bottom electrode. The hysteresis loops of the KNNM<sub>x</sub> films were measured using a ferroelectric test system (Precision Premier II: Radiant Technologies, Inc.). The leakage current–voltage (*I*–*V*) characteristics were measured using an electrometer (Keithley 6517A). The ellipsometric spectral measurements were carried out using a near-infrared to ultraviolet (NIR-UV) SE in the wavelength range of 225–827 nm (1.5–5.5 eV) with a spectral resolution of 5 nm (V-VASE by J. A. Woollam Co., Inc.). The incident angle was selected as 70° for the films corresponding to the experimental optimization near the Brewster angle. As for the variable temperature measurements, the samples were mounted in an Instec cell and the temperature can be set from 300 K to 800 K with a precision of about ±1 K.

### 3 Results and discussion

#### 3.1 Crystal structure

Fig. 1(a) shows the XRD patterns of the KNNM $x$  films in the  $2\theta$  range of  $20\text{--}60^\circ$  at room temperature. All samples are measured using a glancing angle configuration to eliminate the contribution of the substrate. Taking the absence of the standard powder XRD pattern of KNN into consideration, and according to the similar diffraction peaks of the standard powder sample of  $\text{K}_{0.65}\text{Na}_{0.35}\text{NbO}_3$  (JCPDS card No. 77-0038), it can be seen that all of the films show a pure perovskite phase structure. No impurity phase is observed in the films except for the impurity of  $\text{K}_4\text{Nb}_6\text{O}_{17}$ , which was found at the two broad peaks (around  $30^\circ$  and  $40^\circ$ ) when  $x = 0$ . This demonstrates that Mn can enter into the lattice of the KNN perovskite structure.<sup>12,21</sup> KNN is an orthorhombic ( $Amm2$ ) perovskite at room temperature, but it is commonly described with a pseudo-cubic (pc) structure due to the close parameters along different crystallographic orientations of the KNN unit cell.<sup>22</sup> The difference in peak profiles at around  $46^\circ$  in the XRD patterns is usually used as evidence for the phase transition in terms of KNN orthorhombic symmetry.<sup>7</sup> However, the XRD peak at around  $46^\circ$  is so broad, and we do not observe the obvious split peaks, which is in agreement with other studies.<sup>12,19,23–25</sup> This indicates that the KNNM $x$  films have a pc structure. The reasons can be derived from the broadening effects associated with fine crystallite size and strain. Fig. 1(b) and (c) show the supercell of KNN cubic (KNN-C) and orthorhombic (KNN-O) structure, respectively. They were simulated using VESTA software.<sup>26</sup> It can be found that K, Na, Nb and O in KNN-O are displaced along the pseudo-cubic  $[001]$ ,  $[011]$  and  $[111]$  directions relative to those of KNN-C.

#### 3.2 Surface and cross-section morphologies

Fig. 2 shows the surface morphologies of the KNNM $x$  films investigated by AFM. It can be seen that the substrates are covered with nanoparticles of different sizes, which indicates that all films have nanocrystalline growth patterns. The root-mean-square (RMS) surface roughness is 1.87, 1.46, 1.16, 1.14, 1.45 and 1.87 nm for the Mn concentration at  $x = 0, 0.02, 0.04, 0.06, 0.08$  and  $0.10$ , respectively.

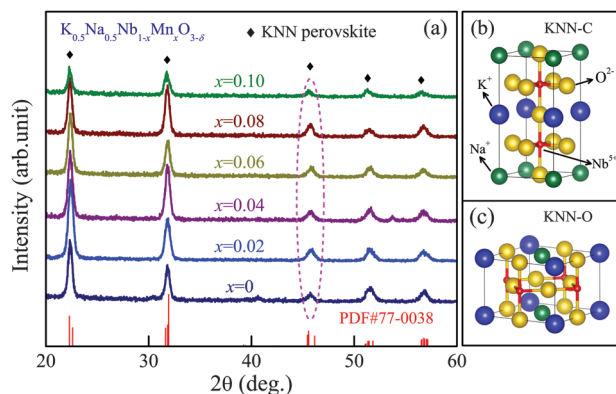


Fig. 1 (a) XRD patterns of the KNNM $x$  ( $x = 0, 0.02, 0.04, 0.06, 0.08$  and  $0.10$ ) films, which were deposited on Pt(111)/Ti/SiO $_2$ /Si(100) substrates. Simulated structures of (b) KNN-C and (c) KNN-O.

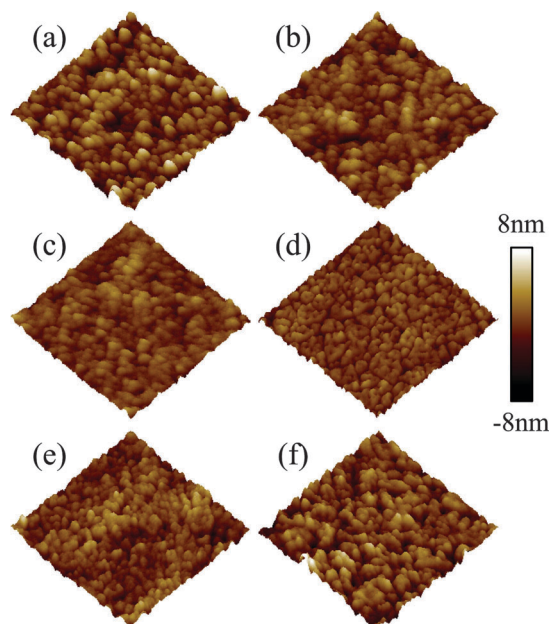


Fig. 2 Three-dimensional AFM images of (a) KNNM0, (b) KNNM0.02, (c) KNNM0.04, (d) KNNM0.06, (e) KNNM0.08 and (f) KNNM0.10, respectively. Note that the scale height is 16 nm, and the measured area is  $1 \times 1 \mu\text{m}^2$ .

0.06, 0.08 and 0.10, respectively. In the case of crystallized films, it is found that the changes in the grain size correspond to the RMS roughness. As examples, the KNNM0 and KNNM0.06 films have the maximum grain size of  $\sim 80$  nm and the minimum grain size of  $\sim 50$  nm, respectively. The AFM images suggest that Mn doping can significantly affect the surface morphology. The remarkable variation can affect the optical and electrical properties, such as lattice vibrations and ferroelectric constants. The cross-sectional FESEM images of the KNNM $x$  films are shown in Fig. 3. It can be observed that there is a distinct interface between the film and substrate. All films are crack-free, uniform and compact. The thickness of all KNNM $x$  films is estimated to be about  $215 \pm 10$  nm.

#### 3.3 Raman scattering

Raman scattering is sensitive to the change in the coordination of local symmetry, which gives information about the molecular vibrations and distortions of the crystal lattice.<sup>27,28</sup> Thus, it can be useful for the compositional and structural analysis in pure and Mn-doped KNN films. Raman spectra of the KNNM $x$  films are shown in Fig. 4. In order to get rid of the trivial temperature dependence, all Raman spectra have been divided by the Bose-Einstein occupation number  $n(\omega) + 1 = 1/[1 - \exp(-\hbar\omega/k_B T)]$  ( $\hbar$  and  $k_B$  are the Planck constant and the Boltzmann constant, respectively). Theoretically, the perovskite structure KNN shows Raman peaks mainly due to the vibrational modes of octahedral  $\text{NbO}_6$ , which shows  $1A_{1g}(\nu_1) + 1E_g(\nu_2) + 2F_{1u}(\nu_3, \nu_4) + F_{2g}(\nu_5) + F_{2u}(\nu_6)$  vibrational modes.<sup>7,28–30</sup> In particular, vibration peaks of the  $\nu_1$  ( $614 \text{ cm}^{-1}$ ) and  $\nu_5$  ( $253 \text{ cm}^{-1}$ ) modes of  $\text{NbO}_6$  are relatively stronger than other modes, which confirms the formation of near-perfect equilateral octahedral symmetry.<sup>31,32</sup> The insets in

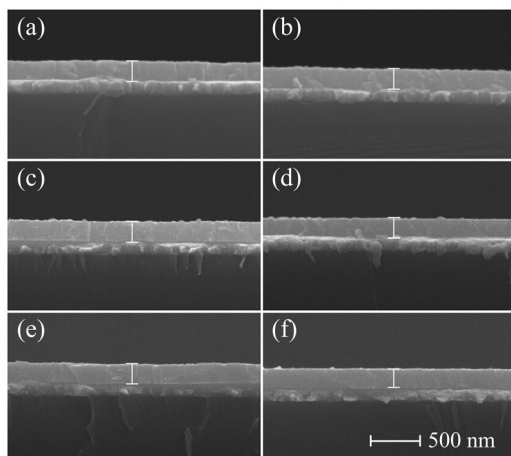


Fig. 3 Cross-sectional FESEM images of (a) KNNM0, (b) KNNM0.02, (c) KNNM0.04, (d) KNNM0.06, (e) KNNM0.08 and (f) KNNM0.10, respectively. Note that the scale bars for all images are 500 nm.

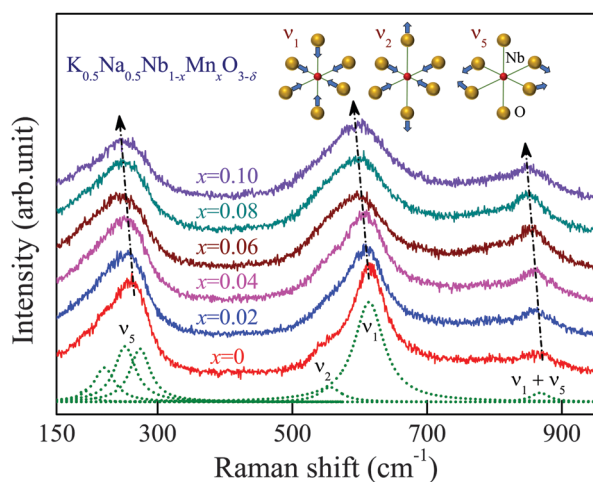


Fig. 4 Raman spectra of the KNNM $x$  ( $x = 0, 0.02, 0.04, 0.06, 0.08$  and  $0.10$ ) films. The arrows show the variation trend of the phonon frequency at about 253, 614 and 870  $\text{cm}^{-1}$ . Note that the dotted lines are the Lorentzian curve fitting for the pure KNN film. The actual fitting parameters of the seven oscillators were 192, 222, 253, 275, 558, 614 and 870  $\text{cm}^{-1}$ . No mathematical smoothing was performed on the experimental data. The insets show the schematic illustrations of three internal vibrational modes of  $\text{NbO}_6$  octahedra, stretching  $\nu_1$  and  $\nu_2$  modes, and bending  $\nu_5$  mode.

Fig. 4 are the schematic illustrations of three internal vibrational modes of  $\text{NbO}_6$  octahedra, stretching  $\nu_1$  and  $\nu_2$  modes, and bending  $\nu_5$  mode.

In order to study the variation trend of phonon modes, Raman spectra were fitted with independent damped harmonic oscillators. It can be seen that incorporation of Mn into KNN causes significant changes in the peak intensity, broadening and position, as shown in Fig. 4. The characteristic frequency of  $\nu_1$ ,  $\nu_5$  and  $\nu_1 + \nu_5$  modes shifts towards lower wavenumbers with increasing Mn concentration. The remarkable shifts originate from the stretching and bending of  $\text{MnO}_6$  ( $\text{Nb}^{5+}$  substitution by  $\text{Mn}^{3+}$ ) octahedra for the KNNM $x$  films. The phenomenon can also be ascribed to the distortion of O–Nb–O angles by

incorporation of Mn ions. It can be concluded that the effect from Mn doping plays an important role in the lattice vibration properties. The present work provides crucial information on the phonon modes of the KNNM $x$  films. It is believed that Mn doping within such a range of concentration is sufficient to find optimal properties for the KNNM $x$  films.

### 3.4 Electrical properties

The typical polarization–electric field ( $P$ – $E$ ) ferroelectric hysteresis loops of the Pt/KNNM $x$ /Pt capacitors were measured at  $f = 1$  kHz and room temperature. The relevant data are shown in Fig. 5. It can be seen that the hysteresis loops of the pure KNN film are not well shaped due to the large leakage current. With increasing Mn concentration, the hysteresis loops become better saturated, while KNNM0.02 and KNNM0.04 still display poor  $P$ – $E$  loops. Nevertheless, the KNNM $x$  ( $0.06 \leq x \leq 0.10$ ) films exhibit well-defined  $P$ – $E$  loops. Fig. 6(a) and (b) show the remanent polarization ( $2P_r$ ) and the coercive field ( $2E_c$ ) of the KNNM $x$  ( $0.04 \leq x \leq 0.10$ ) films, respectively. These data are collected from Fig. 5. It can be concluded that there is an optimal Mn concentration of  $x = 0.06$  for the KNNM $x$  films by taking the shapes of  $P$ – $E$  loops and the values of  $2P_r$  and  $2E_c$  into consideration. This indicates that doping may tend to reach a saturated state at higher Mn doping concentration ( $x > 0.06$ ). This phenomenon can be ascribed to the solubility limit of Mn ions. As we know, low concentration and non-homogeneous distribution of the Mn dopant are consistent with the metal dopant solubility limit found in many niobates.<sup>33</sup> The solubility limit of Mn-doped  $\text{NaNbO}_3$  crystals was found to be  $\sim 5$  mol% Mn.<sup>34</sup> Moreover, co-doping with other ions was proposed to increase the limit. In the present work, the approximate solubility limit of Mn ions was determined to be

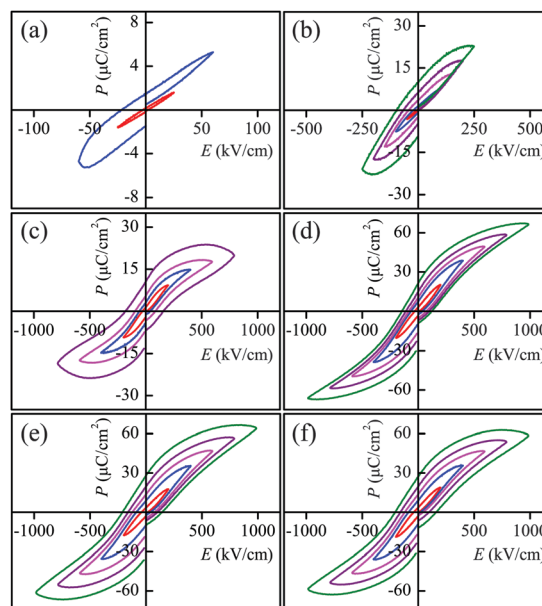
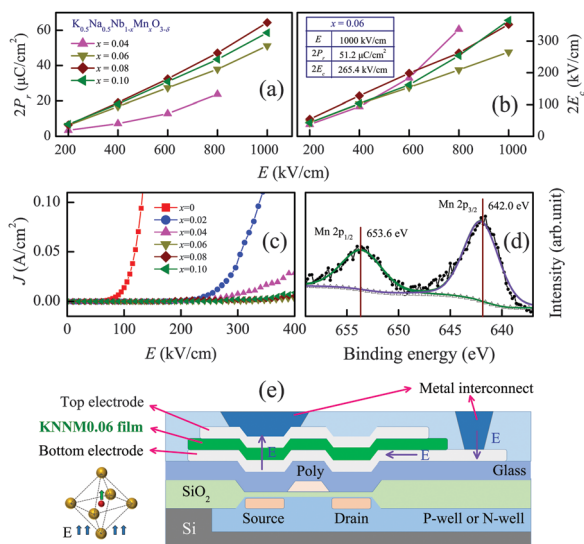


Fig. 5  $P$ – $E$  loops of (a) KNNM0, (b) KNNM0.02, (c) KNNM0.04, (d) KNNM0.06, (e) KNNM0.08 and (f) KNNM0.10, respectively, as a function of the electric field measured at  $f = 1$  kHz and room temperature.



**Fig. 6** (a)  $2P_r$  and (b)  $2E_c$  of the KNNMx ( $x = 0.04, 0.06, 0.08$  and  $0.10$ ) films. The inset table shows the detailed data of  $2P_r$  and  $2E_c$  values for the KNNM0.06 film at the high electric field of  $1000 \text{ kV cm}^{-1}$ . (c) Leakage current density versus electric field ( $J$ - $E$ ) characteristics of the KNNMx ( $x = 0, 0.02, 0.04, 0.06, 0.08$  and  $0.10$ ) films. (d) XPS spectra of the Mn 2p region for the KNNM0.06 film. Note that the dotted and solid lines indicate the experimental data and fitting results, respectively. (e) Schematic diagram of the NVFRAM architecture.

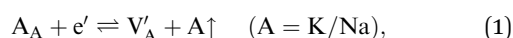
about 6 mol%. The excess Mn ions have little chance to replace Nb ions, but they might occur in the vicinity of structural defects or be pushed out to the crystal surface. As shown in Fig. 6(a) and (b), a relatively large  $2P_r$  of  $51 \mu\text{C cm}^{-2}$  and low  $2E_c$  of  $265 \text{ kV cm}^{-1}$  were obtained for the KNNM0.06 film at an applied electric field of  $1000 \text{ kV cm}^{-1}$ . Although well-saturated  $P$ - $E$  hysteresis loops of Mn-doped KNN films have been reported, those results were obtained for relatively thick films with a thickness of more than  $1.0 \mu\text{m}$ .<sup>12</sup> In this work, KNNM0.06 film shows excellent ferroelectricity under the high electric field of  $1000 \text{ kV cm}^{-1}$  even though the thickness is only about  $215 \text{ nm}$ .

### 3.5 Mechanisms of enhanced ferroelectricity

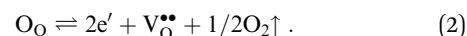
Mn doping was reported to be effective in decreasing the leakage current of KNN crystals.<sup>8</sup> However, it is ambiguous that the Mn ion is substituted at the perovskite A or B site. Moreover, the mechanisms of enhanced ferroelectricity for the KNNMx films should be discussed in detail. Fig. 6(c) shows the leakage current density versus electric field ( $J$ - $E$ ) characteristics of the KNNMx films. As can be seen, the leakage current density increases sharply with increasing applied electric field and decreases with increasing Mn concentration, which indicate that Mn doping can dramatically affect the leakage current. Moreover, the values of the electric field are in agreement with the  $P$ - $E$  loops in Fig. 5. In addition, the chemical state of the Mn element for the KNNMx films was investigated by using the XPS technique. The XPS data were fitted using XPS PEAK software, and the final fitting curves were taken as 20% Lorentzian and 80% Gaussian. As an example, high-resolution XPS spectra of Mn 2p for the KNNM0.06 film and its fitting

results are presented in Fig. 6(d). It should be noted that the Mn 2p XPS spectra were observed at  $642.0 \text{ eV}$  and  $653.6 \text{ eV}$  for the  $2p_{3/2}$  and  $2p_{1/2}$  peaks, respectively. This unquestionably suggests that the Mn ion is mostly in the  $3+$  valence state, which is in good agreement with the findings in the core level spectra of  $\text{Mn}_2\text{O}_3$ .<sup>35</sup> Taking the effects of expanded lattice volume by Mn substitution and the similar ionic-size between  $\text{Nb}^{5+}$  ( $0.64 \text{ \AA}$ ) and  $\text{Mn}^{3+}$  ( $0.65 \text{ \AA}$ ) into consideration,<sup>36</sup> it suggests that the majority of Mn ions are substituted at the  $\text{Nb}^{5+}$  site as  $\text{Mn}^{3+}$ . Moreover, the Mn element at the perovskite B site has been observed for some ferroelectric oxides, such as  $\text{BiFeO}_3$ ,<sup>18</sup>  $\text{BaTiO}_3$ ,<sup>16</sup> and  $\text{K}_{0.5}\text{Na}_{0.5}\text{NbO}_3$ .<sup>8,37</sup> The increased valence of the Mn ion plays an important role in electron-hole absorption during oxidation.<sup>8,12,21</sup>

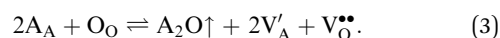
As we know, alkali ions are easy to volatilize ( $\uparrow$ ) during the pyrolysis process. Therefore, alkaline ion vacancies ( $V'_A$ ) would be formed, which can be expressed by eqn (1):



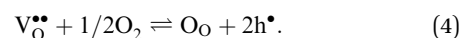
accompanied by the formation of oxygen vacancies, which can be expressed by eqn (2):



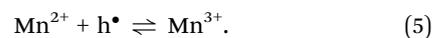
The electron ( $e'$ ) in eqn (1) was derived from eqn (2). The absorption of  $e'$  in eqn (1) would promote the balance of eqn (2) to the right. As a result, the  $V'_A$  and  $V_O^{\bullet\bullet}$  would coexist. Eqn (1) and (2) can be briefly expressed as:



The excess  $\text{K}^+$  and  $\text{Na}^+$  in the starting composition would compensate the alkaline ion vacancies in order to ensure an accurate stoichiometric ratio. During high temperature annealing, the KNNMx films absorb oxygen into the lattice, which can be expressed by:



The oxygen occupies  $V_O^{\bullet\bullet}$  as  $\text{O}_O$  accompanied by the formation of  $2h^{\bullet}$ . The  $h^{\bullet}$  represents free carrier holes. However, the introduction of  $\text{Mn}^{2+}$  can absorb these holes by increasing the valence of  $\text{Mn}^{2+}$  as expressed by:



Therefore, the introduction of Mn ions can effectively reduce the amount of oxygen vacancies and holes.<sup>8</sup> As a result, the KNNM0.06 film shows well-saturated  $P$ - $E$  hysteresis loops.

Another reason can be ascribed to the morphology of grain accumulation. Generally, extended defects in polycrystalline metal oxide films, such as grains and grain boundaries (GBs), are thought to play an important role in determining their electrical characteristics.<sup>38</sup> As an example, compared with the KNNM0 film, the KNNM0.06 film has a smoother surface and a smaller interval between two grains with the minimum RMS surface roughness. It is believed that the leakage current through the KNNMx film preferentially flows *via* the GBs, which

provide preferential percolation paths for electron transport. As a result, the KNNM0.06 film shows better electric insulativity.

In addition to the above two factors, the effect due to the 3d orbital of Mn might be another influencing factor. It is known that bond hybridizations between O 2p and metal 3d or 4d orbitals trigger soft mode behavior and lead to ferroelectricity.<sup>39,40</sup> The 3d orbital of Mn would take part in the hybridization with the 2p orbital of O, just like the hybridization of O 2p and Nb 4d. From the perspective of valence bonds and atomic orbitals, it is understandable that Mn doping can dramatically affect the ferroelectricity of the KNNM $x$  films.

In consideration of the excellent ferroelectric properties of the KNNM0.06 film, it might be used to design the nonvolatile ferroelectric random-access memory (NVFRAM). Fig. 6(e) shows the schematic diagram of the NVFRAM architecture. The KNNM0.06 ferroelectric film was placed on the conventional semiconductor process layers. The mechanism of ferroelectric memory can be depicted as follows. An electric field is applied across the KNNM0.06 crystal with the top and bottom electrodes. The central Nb atom would move up or down based on the direction of the electric field thereby setting a digital data state (0 or 1). After reading, the position of the atom is restored. Writing also follows the same operation, but new data are restored instead of old data.

### 3.6 Ellipsometric spectra

As we all know, SE is a sensitive and non-destructive method to extract simultaneously optical constants and thicknesses of multilayer films. It measures the relative changes in the amplitude  $\Psi(E)$  and phase  $\Delta(E)$  of particular directions polarized lights upon oblique reflection from the sample surface.<sup>15,20</sup> Note that  $\Psi(E)$  and  $\Delta(E)$  are the functions of the incident angle, photon energy, film thickness and optical constants. In the present work, the SE technique was used to extract the dielectric functions  $[\tilde{\epsilon}(E) = \epsilon_r(E) + i\epsilon_i(E)]$  and other physical parameters of the KNNM $x$  films with a four-phase layered structure (air/surface rough layer (SRL)/KNNM $x$  film/Pt substrate). With regard to wide band gap semiconductor materials, the complex dielectric function  $\tilde{\epsilon}(E)$  can be expressed by the Adachi model, which is based on the KKT and connected with the electronic band structure. The method reveals the distinct structures at the energy of the  $M_1$ -type critical point, which is written as:<sup>41</sup>

$$\tilde{\epsilon}(E) = \epsilon_\infty - A_0 \ln(1 - \chi_0^2)/\chi_0^2 \quad (6)$$

$$\chi_0 = (E + i\Gamma_0)/E_g \quad (7)$$

Here,  $\epsilon_\infty$  is the high-frequency dielectric constant,  $A_0$  and  $\Gamma_0$  are the strength and broadening values of the optical band gap ( $E_g$ ) transition, respectively. The thickness of film ( $d_f$ ) and SRL ( $d_s$ ),  $E_g$  and  $\epsilon_\infty$  could be extracted from the best fit between the experimental and theoretical spectra. Correspondingly, the optical constants  $[\tilde{N}(E) = n(E) + i\kappa(E)$ , refractive index ( $n$ ) and extinction coefficient ( $\kappa$ )] can be calculated from the well-known relationship  $\tilde{N}(E) = \sqrt{\tilde{\epsilon}(E)}$ .

Fig. 7(a) and (b) show the experimental and fitted ellipsometric spectra [ $\Psi(E)$  and  $\Delta(E)$ ] of the KNNM $x$  films, respectively.

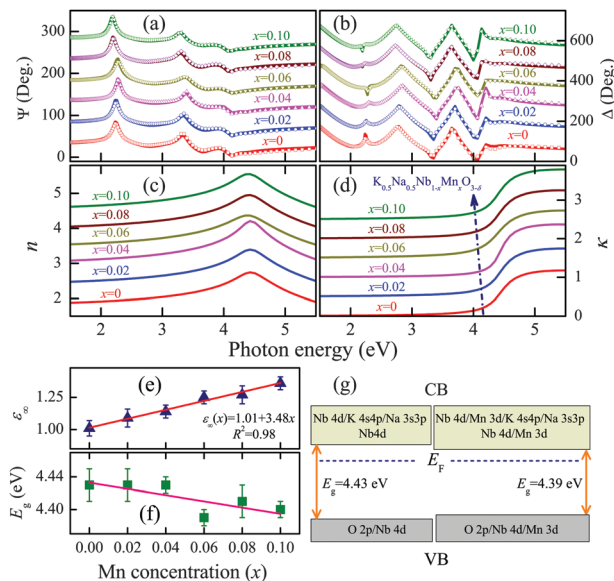


Fig. 7 The NIR-UV experimental (dotted lines) and best-fitted (solid lines) ellipsometric spectra (a)  $\Psi(E)$  and (b)  $\Delta(E)$  of the KNNM $x$  ( $x = 0, 0.02, 0.04, 0.06, 0.08$  and  $0.10$ ) films. Evolution of the (c) refractive index ( $n$ ) and (d) extinction coefficient ( $\kappa$ ) of the KNNM $x$  ( $x = 0, 0.02, 0.04, 0.06, 0.08$  and  $0.10$ ) films in the photon energy range of 1.5–5.5 eV. For clarity, the arrow indicates the absorption edge redshift with increasing Mn concentration. Note that  $\Psi$ ,  $\Delta$ ,  $n$  and  $\kappa$  are vertically shifted by adding 50, 100, 0.5 and 0.5, respectively. Composition dependent (e)  $\epsilon_\infty$  and (f)  $E_g$  of the KNNM $x$  films. The solid lines represent the linearly fitted results. (g) Schematic representation of the electronic band structure for the KNNM0 and KNNM0.06 films, where  $E_f$  denotes the Fermi energy level.

As can be seen, a good agreement is obtained between the experimental and fitted spectra in the entirely measured photon energy range of 1.5–5.5 eV. It confirms that the dielectric function model used in the present work is reasonable to describe the optical dispersion behavior of the KNNM $x$  films. The interference patterns due to the multi-reflectance between the film and Pt substrate are observed below the photon energy of  $\sim 4.4$  eV. In addition, the fitted model parameter values ( $\epsilon_\infty$ ,  $A_0$ ,  $E_g$ ,  $\Gamma_0$ ,  $d_s$  and  $d_f$ ) are summarized in Table 1. The values of surface roughness and thickness of the KNNM $x$  films are similar to the data derived from the AFM and SEM data. This indicates that the selected Adachi dielectric function model and the four-phase structure can be reasonable and acceptable for the KNNM $x$  films.

The  $n$  and  $\kappa$  of the KNNM $x$  films are shown in Fig. 7(c) and (d), respectively. It can be seen that the  $n$  increases and approaches the maximum at about 4.4 eV with increasing photon energy, and then decreases due to the well-known Van Hove singularities. In the transparent region ( $E < E_g$ ), the  $\kappa$  is closer to zero and then remarkably increases as the photon energy further increases beyond the fundamental band gap. This suggests that a strong optical absorption appears, which shows the interband electronic transition from the top of the valence band to the bottom of the conduction band for the KNNM $x$  films. As shown in Fig. 7(d), the absorption edge shifts towards the lower photon energy side with increasing Mn concentration.

**Table 1** Parameter values of the Adachi dielectric function model for the KNNMx films determined from the simulation of ellipsometric spectra in Fig. 7(a) and (b). Note that 95% reliability of the fitting parameters is given with ( $\pm$ )

Sample	$\epsilon_\infty$	$A_0$	$\Gamma_0$ (eV)	$E_g$ (eV)	$d_s$ (nm)	$d_f$ (nm)
KNNM0	1.01 $\pm$ 0.06	2.38 $\pm$ 0.08	0.185 $\pm$ 0.006	4.43 $\pm$ 0.02	7.2 $\pm$ 0.9	225.8 $\pm$ 2.8
KNNM0.02	1.09 $\pm$ 0.07	2.64 $\pm$ 0.05	0.181 $\pm$ 0.004	4.43 $\pm$ 0.02	2.8 $\pm$ 0.5	212.2 $\pm$ 1.6
KNNM0.04	1.14 $\pm$ 0.05	3.00 $\pm$ 0.05	0.130 $\pm$ 0.005	4.43 $\pm$ 0.01	2.6 $\pm$ 0.4	193.6 $\pm$ 1.4
KNNM0.06	1.25 $\pm$ 0.05	2.76 $\pm$ 0.03	0.230 $\pm$ 0.005	4.39 $\pm$ 0.01	1.8 $\pm$ 0.6	199.9 $\pm$ 1.2
KNNM0.08	1.27 $\pm$ 0.07	2.77 $\pm$ 0.05	0.192 $\pm$ 0.005	4.41 $\pm$ 0.02	7.6 $\pm$ 0.6	204.5 $\pm$ 1.6
KNNM0.10	1.36 $\pm$ 0.05	2.94 $\pm$ 0.03	0.189 $\pm$ 0.005	4.40 $\pm$ 0.01	2.4 $\pm$ 0.4	199.2 $\pm$ 1.3

The Adachi model parameter  $E_g$  and  $\epsilon_\infty$  with their fitted values are shown in Fig. 7(e) and (f), respectively. It can be seen that  $\epsilon_\infty$  increases with increasing Mn concentration and it can be expressed by the linear relationship:  $1.01 + 3.48x$ . The  $\epsilon_\infty$  accounts for the so-called high frequency limit. The results indicate that the contributions from the high-energy interband transitions become more prominent with increasing Mn concentration. In addition, the  $E_g$  slightly decreases with increasing Mn concentration. The average  $E_g$  of the KNNMx films is 4.41 eV. It should be emphasized that the values are much larger than that derived by the theoretical calculation (1.6 eV) and other experimental results (3.5 eV).<sup>42,43</sup> The reasons can be ascribed to the huge stress and imperfect crystallinity of the thinner KNNMx films. A similar enlarged band gap was also observed in other ferroelectric oxides.<sup>44</sup> The band gap of KNN-based film prepared by Yao *et al.* is determined to be  $\sim 4.5$  eV.<sup>45</sup> Rani *et al.* also obtained a wide band gap of  $\sim 4.3$  eV in pure KNN ceramics.<sup>46</sup> From the viewpoint of KNN-based capacitor devices, photocatalysts and ultraviolet detectors, a wider optical band gap material can be suitable for these potential applications. In the present work, the Mn doping did not dramatically change the band gap of the KNN films. Theoretically, the valence band (VB) of KNN is dominated by the strong hybridization of O 2p and Nb 4d. In the conduction band (CB), the lower energy band states are mainly dominated by Nb 4d, and the higher energy band states mainly correspond to the Nb 4d, Na 3s3p and K 4s4p states.<sup>42</sup> In addition, the localization degree of d electron states is  $3d > 4d > 5d$ .<sup>47</sup> As a result, the 3d orbital of the Mn element cannot effectively broaden the Nb 4d states and further reduce the band gap energy, which is in agreement with the results of the present work. A relevant model of electronic band structure was presented to explain and visualize the effects of Mn doping, as shown in Fig. 7(g). Although Mn doping has a little effect on the band gap of KNN films, it can dramatically decrease the leakage current and enhance the ferroelectricity. We believe that the optimal ferroelectric properties of Mn doping described in this work will open new avenues for developing KNNM0.06-based films for potential multifunctional applications.

In addition, in order to further investigate the optical dispersion behavior of the KNNMx films, as an example, temperature dependent dielectric functions of the KNNM0.06 film in the photon energy range of 1.5–5.5 eV have been investigated by SE from 300 K to 800 K using the idem Adachi model. Fig. 8(a) shows the experimental ellipsometric spectra  $\Psi(E)$  and  $\Delta(E)$  of the KNNM0.06 film at 300 K and 800 K. It can be seen that there is an obvious variation in the raw experimental spectra.

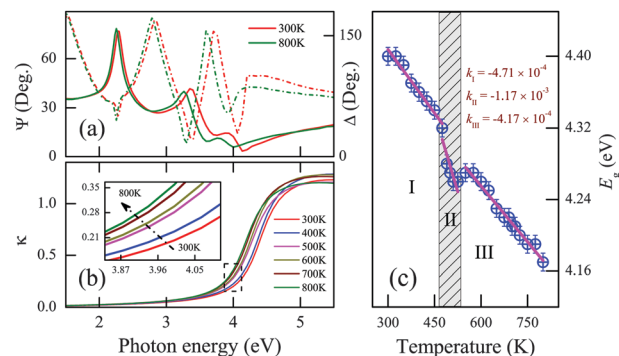


**Fig. 8** (a) The temperature dependent NIR-UV experimental ellipsometric spectra  $\Psi(E)$  (solid lines) and  $\Delta(E)$  (dash lines) of the KNNM0.06 film at 300 K and 800 K. (b) Evolution of the extinction coefficient ( $\kappa$ ) of the KNNM0.06 film with increasing temperature. The inset shows the enlargement of the dashed box, for clarity, the arrow indicates the trend of temperature from 300 K to 800 K. (c)  $E_g$  evolution of the KNNM0.06 film as a function of temperature. Note that the solid lines represent the linearly fitted results. The shadow pattern corresponds to the phase change region.  $k_I$ ,  $k_{II}$  and  $k_{III}$  are the  $dE_g/dT$  values of part I, II and III, respectively.

Fig. 8(b) shows the evolution of the extinction coefficient ( $\kappa$ ) of the KNNM0.06 film with increasing temperature. It is found that the features of  $\kappa$  show an abrupt variation near 500 K and 700 K. To clarify the evolution of the electronic structure, the  $E_g$  as a function of temperature for the KNNM0.06 film was plotted in Fig. 8(c). The variations of  $E_g$  were caused by temperature effects and can be separated into three parts. Each part was linearly fitted, and the corresponding temperature coefficients ( $dE_g/dT$ ,  $k_I$ ,  $k_{II}$  and  $k_{III}$ ) are shown in Fig. 8(c). As can be seen, part II is quite different, the  $E_g$  has an abrupt variation near 500 K, which can be related to phase transition. Generally, the ferroelectric phase transition is related to electronic band variation. KNN shows several phase transitions similar to  $\text{KNbO}_3$  with increasing temperature.<sup>48</sup> Pure  $\text{KNbO}_3$  has the following polymorphisms, the low-temperature (lesser than 263 K) rhombohedral (R) phase, the room-temperature orthorhombic (O) phase, and the high-temperature tetragonal (T, 498–708 K) and cubic (C,  $>708$  K) phases.<sup>6</sup> As we all know, the phase transition of KNN can be detected by several methods, such as X-ray diffraction (XRD) and electrical testing. However, there are few reports on phase transition using non-destructive spectroscopic optical methods. It has been widely accepted that spectral response is representative of the interband and intraband transitions.<sup>49,50</sup> In this work, the phase transition of the KNNM0.06 film is revealed with the aid of dielectric

function analysis. It should be emphasized that the value of  $k_{\text{II}}$  is much larger than  $k_{\text{I}}$  and  $k_{\text{III}}$ . This indicates that there is an obvious phase transition (O  $\rightarrow$  T) around 500 K. However, the variation of  $E_{\text{g}}$  around 700 K is slight, it did not indicate the absence of phase transition (T  $\rightarrow$  C) around 700 K, which can be observed in the evolution of extinction coefficient ( $\kappa$ ), as shown in Fig. 8(b).

### 3.7 Domain behavior

In view of the excellent ferroelectric properties of the KNNM0.06 film, it is necessary to investigate its ferroelectric domain behavior, which may be pivotal to the enhancement of electro-mechanical properties.<sup>9</sup> Generally, PFM could be a very powerful tool for understanding the physical behavior of piezoresponsive materials.<sup>51,52</sup> In this work, we investigate the domain behavior of the KNNM0.06 film for further understanding its piezoelectric and ferroelectric properties. Fig. 9(a) shows the schematic illustration of PFM measurements. Considering that the insulating Si layer can interdict the voltage signal between the tip and the platform, the conductive silver paste is utilized to glue the exposed Pt layer and the metal sheet.

PFM experiments are conducted in both lateral and vertical modes in order to analyze the polarization orientation. The tip was scanned in contact mode with the application of a voltage between the tip and bottom electrodes. Thus, both in-plane polarization (IPP) and out-of-plane polarization (OPP) images

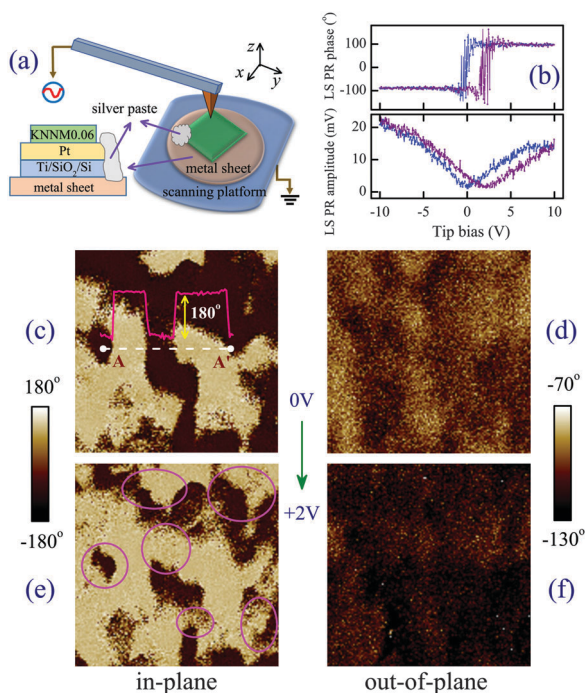


**Fig. 9** (a) Schematic illustration of PFM measurement. (b) LS PR phase and amplitude vs. tip bias graphs for the KNNM0.06 film. The phase of (c) IPP and (d) OPP signals at the tip bias of 0 V for the KNNM0.06 film. Note that the inset shows the section analysis of the IPP image based on the AA' area. The phase of (e) IPP and (f) OPP signals at the tip bias of +2 V for the KNNM0.06 film. Note that the circular areas indicate the evident switching of the IPP domain, and the measured area is  $1 \times 1 \mu\text{m}^2$ .

can be obtained due to the converse piezoelectric effect. IPP and OPP show the polarization parallel to and perpendicular to the sample surface, respectively. It could be possible to reconstruct the axis orientation of the KNN crystal by using IPP and OPP images.<sup>32,53</sup> Moreover, compared with the OPP image, the IPP image shows a better signal to noise ratio due to specific measuring conditions. For the unpolarized orthorhombic KNN crystal, it provides 12 possible spontaneous polarization vectors in all [110] directions.<sup>54</sup> The angles between two polarization vectors can be  $60^\circ$ ,  $90^\circ$ ,  $120^\circ$  or  $180^\circ$ , which indicates that there are  $60^\circ$ ,  $90^\circ$ ,  $120^\circ$  or  $180^\circ$  domains for the orthorhombic KNN crystal.

In the meantime, the ramp mode in the piezoresponse (PR) mode was used to help us understand the physical nature of the KNNM0.06 film. As shown in Fig. 9(b), the low speed (LS) PR phase plot shows the hysteresis loop of the KNNM0.06 film by applying a ramp voltage loop from  $-10$  V to  $10$  V. The well-defined rectangular phase hysteresis loop reflects good PR properties. The LS PR amplitude plot shows the amplitude of oscillation, which allows estimation of the piezoelectric coefficients. The piezoelectric coefficient  $d_{33}$  of the KNNM0.06 film can be calculated by using the following formula:  $d_{33} = \text{LS PR amplitude (mV)} \times \text{deflection sensitivity (nm V}^{-1})/16/\text{LS PR AC bias (V)}$ . It can be seen that there is a shift of the curves to positive bias voltage, which may be caused by surface and space charge. In addition, by means of the lateral and vertical modes, the phase signals of IPP and OPP have been recorded, which carry information on the polarization direction. The tip bias of 0 V and +2 V was used to investigate the domain behavior. When the tip bias is 0 V, a clear domain contrast can be observed in the in-plane direction, as shown in Fig. 9(c). The smallest observed domains are located in the size of several hundreds of nanometers. Moreover, the inset curve in Fig. 9(c) shows the section analysis of the IPP image based on the AA' area. It can be seen that the difference value of the phase between the bright and dark areas is about  $180^\circ$ , which indicates that the KNNM0.06 film has the  $180^\circ$  domain. However, the OPP image shows a very low contrast, which can be described as a single domain for simplicity, as shown in Fig. 9(d). The phenomenon can be ascribed to the electric field effects, which were derived from the conductive Pt layer. In addition, after the application of the +2 V field, switching of the in-plane polarization domain was evident, as shown in the circular areas of Fig. 9(e). An obvious change is also found in the OPP image, as shown in Fig. 9(f). It still shows a very low contrast but has a darker area, which is in agreement with the direction of the applied electric field. By combining the study of IPP and OPP images, it is clear that the KNNM0.06 film, which is deposited on the Pt(111)/Ti/SiO<sub>2</sub>/Si(100) substrate, mainly shows the in-plane ( $180^\circ$ ) nano-domain.

## 4 Conclusion

In summary, high-quality KNNM $x$  films ( $\sim 215$  nm, RMS < 2 nm) have been prepared. Mn doping can dramatically lower  $E_{\text{c}}$ , improve  $P_{\text{r}}$  and affect the phonon modes. There is an optimal Mn

concentration of  $x = 0.06$ . The Mn ions are mostly in the 3+ valence state and mainly replace niobium ions. The mechanisms of enhanced ferroelectricity can be ascribed to the increased valence of the Mn ion, and the effects of the GBs. Moreover, the KNNM0.06 film has good piezoresponse properties and mainly shows the distinct in-plane ( $180^\circ$ ) nano-domains. In addition, the Adachi dielectric function model and a four-phase layered model were successfully applied to fit the measured ellipsometric spectra and reasonably described the optical dispersion behavior of the KNNM $x$  films. The anomaly of electronic band transitions during the phase transition has been discussed in detail. In consideration of the excellent properties of the KNNM0.06 film, it can be a novel idea to develop KNNM0.06-based films for potential multifunctional applications, for instance, co-doping with rare earth elements.

## Acknowledgements

The work was financially supported by Major State Basic Research Development Program of China (Grant No. 2011CB922200 and 2013CB922300), the Natural Science Foundation of China (Grant No. 11374097 and 61376129), Projects of Science and Technology Commission of Shanghai Municipality (Grant No. 14XD1401500, 13JC1402100, and 13JC1404200), and the Program for Professor of Special Appointment (Eastern Scholar) at Shanghai Institutions of Higher Learning.

## References

- 1 A. S. Mischenko, Q. Zhang, J. F. Scott, R. W. Whatmore and N. D. Mathur, *Science*, 2006, **311**, 1270–1271.
- 2 M. Ahart, M. Somayazulu, R. E. Cohen, P. Ganesh, P. Dera, H. K. Mao, R. J. Hemley, Y. Ren, P. Liermann and Z. G. Wu, *Nature*, 2008, **451**, 545–548.
- 3 E. Cross, *Nature*, 2004, **432**, 24–25.
- 4 C. Reitz, P. M. Leufke, H. Hahn and T. Brezesinski, *Chem. Mater.*, 2014, **26**, 2195–2202.
- 5 Y. Saito, H. Takao, T. Tani, T. Nonoyama, K. Takatori, T. Homma, T. Nagaya and M. Nakamura, *Nature*, 2004, **432**, 84–87.
- 6 J. F. Li, K. Wang, F. Y. Zhu, L. Q. Cheng, F. Z. Yao and D. J. Green, *J. Am. Ceram. Soc.*, 2013, **96**, 3677–3696.
- 7 F. Bortolani, A. D. Campo, J. F. Fernandez, F. Clemens and F. Rubio-Marcos, *Chem. Mater.*, 2014, **26**, 3838–3848.
- 8 Y. Kizaki, Y. Noguchi and M. Miyayama, *Appl. Phys. Lett.*, 2006, **89**, 142910.
- 9 F. Z. Yao, K. Wang, L. Q. Cheng, X. D. Zhang, W. Zhang, F. Y. Zhu and J. F. Li, *J. Am. Ceram. Soc.*, 2015, **98**, 448–454.
- 10 C. R. Cho and A. Grishin, *J. Appl. Phys.*, 2000, **87**, 4439.
- 11 K. Shibata, F. Oka, A. Ohishi, T. Mishima and I. Kanno, *Appl. Phys. Express*, 2008, **1**, 011501.
- 12 L. Y. Wang, W. Ren, P. Shi and X. Q. Wu, *J. Appl. Phys.*, 2014, **115**, 034103.
- 13 R. W. Schwartz, *Chem. Mater.*, 1997, **9**, 2325–2340.
- 14 M. Li, M. J. Pietrowski, R. A. D. Souza, H. R. Zhang, I. M. Reaney, S. N. Cook, J. A. Kilner and D. C. Sinclair, *Nat. Mater.*, 2014, **13**, 31–35.
- 15 S. Zhang, M. J. Han, J. Z. Zhang, Y. W. Li, Z. G. Hu and J. H. Chu, *ACS Appl. Mater. Interfaces*, 2013, **5**, 3191–3198.
- 16 J. Y. Son, J. H. Lee, S. Song, Y. H. Shin and H. M. Jang, *ACS Nano*, 2013, **7**, 5522–5529.
- 17 Y. Yoneda, Y. Kitanaka, Y. Noguchi and M. Miyayama, *Phys. Rev. B: Condens. Matter Mater. Phys.*, 2012, **86**, 184112.
- 18 J. Z. Zhang, Z. H. Duan, H. Zhang, M. J. Han, Y. W. Li, Z. G. Hu and J. H. Chu, *J. Mater. Chem. C*, 2013, **1**, 6252–6258.
- 19 J. Park, S. S. Won, C. W. Ahn, I. W. Kim and G. L. Brennecke, *J. Am. Ceram. Soc.*, 2013, **96**, 146–150.
- 20 J. Z. Zhang, X. G. Chen, Y. D. Shen, Y. W. Li, Z. G. Hu and J. H. Chu, *Phys. Chem. Chem. Phys.*, 2011, **13**, 13096–13105.
- 21 S. Y. Lee, C. W. Ahn, A. Ullah, H. J. Seog, J. S. Kim, S. H. Bae and I. W. Kim, *Curr. Appl. Phys.*, 2011, **11**, S266–S269.
- 22 K. Wang and J. F. Li, *Appl. Phys. Lett.*, 2007, **91**, 262902.
- 23 K. Tanaka, H. Hayashi, K. I. Kakimoto, H. Ohsato and T. Iijima, *Jpn. J. Appl. Phys.*, 2007, **46**, 6964–6970.
- 24 Z. G. Yi, Y. Liu, M. A. Carpenter, J. Schiemer and R. L. Withers, *Dalton Trans.*, 2011, **40**, 5066–5072.
- 25 Q. Yu, J. F. Li, W. Sun, Z. Zhou, Y. Xu, Z. K. Xie, F. P. Lai and Q. M. Wang, *J. Appl. Phys.*, 2013, **113**, 024101.
- 26 K. Momma and F. Izumi, *J. Appl. Crystallogr.*, 2008, **41**, 653–658.
- 27 J. Z. Zhang, W. Y. Tong, J. J. Zhu, J. Y. Xu, Z. H. Duan, L. P. Xu, Z. G. Hu, C. G. Duan, X. J. Meng, Z. Q. Zhu and J. H. Chu, *Phys. Rev. B: Condens. Matter Mater. Phys.*, 2015, **91**, 085201.
- 28 M. A. Rafiq, P. Supancic, M. E. Costa, P. M. Vilarinho and M. Deluca, *Appl. Phys. Lett.*, 2014, **104**, 011902.
- 29 Z. Wang, H. S. Gu, Y. M. Hu, K. Yang, M. Z. Hu, D. Zhou and J. G. Guan, *CrystEngComm*, 2010, **12**, 3157–3162.
- 30 K. I. Kakimoto, K. Akao, Y. P. Guo and H. Ohsato, *Jpn. J. Appl. Phys.*, 2005, **44**, 7064–7067.
- 31 L. Q. Cheng, K. Wang, Q. Yu and J. F. Li, *J. Mater. Chem. C*, 2014, **2**, 1519–1524.
- 32 G. Ray, N. Sinha, S. Bhandari, B. Singh, I. Bdikin and B. Kumar, *CrystEngComm*, 2014, **16**, 7004–7012.
- 33 A. Molak and J. Kubacki, *Cryst. Res. Technol.*, 2001, **36**, 893–902.
- 34 L. A. Reznitchenko, N. V. Dergunova, G. A. Geguzina, O. N. Razumovskaya, L. A. Shilkina and L. S. Ivanova, *Ferroelectrics*, 1998, **214**, 241–254.
- 35 G. C. Allen, S. J. Harris, J. A. Jutson and J. M. Dyke, *Appl. Surf. Sci.*, 1989, **37**, 111–134.
- 36 R. D. Shannon, *Acta Crystallogr., Sect. A: Cryst. Phys., Diffraction, Theor. Gen. Crystallogr.*, 1976, **32**, 751–767.
- 37 Y. Inagaki, K. I. Kakimoto and I. Kagomiya, *J. Eur. Ceram. Soc.*, 2010, **30**, 301–306.
- 38 O. Pirrotta, L. Larcher, M. Lanza, A. Padovani, M. Porti, M. Nafria and G. Bersuker, *J. Appl. Phys.*, 2013, **114**, 134503.
- 39 J. F. Scott, *Rev. Mod. Phys.*, 1974, **46**, 83–128.
- 40 A. Bussmann-Holder, *Phys. B*, 1999, **263–264**, 408–411.
- 41 S. Adachi, *Phys. Rev. B: Condens. Matter Mater. Phys.*, 1987, **35**, 7454.

- 42 S. L. Zhou, X. Zhao, X. P. Jiang and X. D. Han, *Chin. J. Struct. Chem.*, 2012, **31**, 1095–1104.
- 43 G. H. Khorrami, A. Kompany and A. K. Zak, *Adv. Powder Technol.*, 2015, **26**, 113–118.
- 44 Y. B. Yao, W. C. Liu, C. L. Mak and K. H. Wong, *AIP Adv.*, 2011, **1**, 032172.
- 45 Y. B. Yao, H. T. Chan, C. L. Mak and K. H. Wong, *Thin Solid Films*, 2013, **537**, 156C162.
- 46 J. Rani, P. K. Patel, N. Adhlakha, H. Singh and K. L. Yadav, *J. Mater. Sci. Technol.*, 2014, **30**, 459–465.
- 47 S. S. P. Parkin, *Phys. Rev. Lett.*, 1991, **67**, 3598.
- 48 H. J. Trodahl, N. Klein, D. Damjanovic, N. Setter, B. Ludbrook, D. Rytz and M. Kuball, *Appl. Phys. Lett.*, 2008, **93**, 262901.
- 49 S. Zhang, J. Z. Zhang, M. J. Han, Y. W. Li, Z. G. Hu and J. H. Chu, *Appl. Phys. Lett.*, 2014, **104**, 041106.
- 50 S. Guo, X. J. Ding, J. Z. Zhang, Z. G. Hu, X. L. Ji, L. C. Wu, Z. T. Song and J. H. Chu, *Appl. Phys. Lett.*, 2015, **106**, 052105.
- 51 D. J. Kim, T. R. Paudel, H. D. Lu, J. D. Burton, J. G. Connell, E. Y. Tsybal, S. S. A. Seo and A. Gruverman, *Adv. Mater.*, 2014, **26**, 7660–7665.
- 52 R. J. Xu, J. Karthik, A. R. Damodaran and L. W. Martin, *Nat. Commun.*, 2014, **5**, 3120.
- 53 Y. C. Huang, Y. Y. Liu, Y. T. Lin, H. J. Liu, Q. He, J. Y. Li, Y. C. Chen and Y. H. Chu, *Adv. Mater.*, 2014, **26**, 6335–6340.
- 54 R. P. Herber, G. A. Schneider, S. Wagner and M. J. Hoffmann, *Appl. Phys. Lett.*, 2007, **90**, 252905.